A Scheme for Target Tracking and Pointing During Small Celestial Body Encounters

Garry M. Burdick,* Ho-Sen Lin,† and Edward C. Wong‡
Jet Propulsion Laboratory, California Institute of Technology, Pasadena, California

A scheme has been developed and simulated for closed-loop tracking and pointing space-borne science instruments at small celestial bodies such as comets and asteroids during high-velocity encounters. To overcome ephemeris uncertainties for these bodies, the scheme involves sequential estimation of flyby model parameters. The design consists of a two-axis gimbaled platform mounted on a three-axis stabilized spacecraft. A platform-mounted optical tracker provides target direction measurements, while precision microstep actuators enable high-rate platform slewing. For comet missions which involve dust particle impact disturbances, a dual-mode attitude control scheme is presented for minimizing transient response time.

Introduction

SEVERAL future deep space missions planned for the 1990's and beyond require precise pointing of science instruments at small celestial bodies. Missions involving flyby encounters with comets, asteroids, and small planetary moons fall into this category. Prior deep space missions have pointed science instruments open-loop. This has been possible because precise target vectors could be precalculated and line-of-sight rates have been small, relative to required instrument integration durations. For small celestial body missions, though, the size of these objects dictates relatively close or low-altitude aimpoints, typically less than 1000 km. For some comet missions, the close aimpoint and high relative velocity (~60 km/s) combine to result in peak tracking rates of several degrees per second. Furthermore, trajectory uncertainty of these objects relative to the spacecraft dictates that the pointing system include the capability to close the loop with respect to the measured target direction. Finally, the hostile dust environment near comets presents special difficulty for a precision pointing system and fragile instruments. Reference 1 presents more information about comet flyby missions.

This paper presents the design and analysis of a closed-loop pointing system that satisfies the tight pointing requirements envisioned for these small body missions.

System Description and Overview

The pointing system described in this paper consists of a two-axis gimbaled science platform mounted on a three-axis stabilized spacecraft. The science platform carries cameras and other instruments that must be pointed at the small body under observation. Typically, the cameras place the most stringent requirements on the pointing system. Accuracies on the order of 1 mrad and pointing stability or jitter less than 10 μrad during an image integration interval of 5 ms are typical requirements.

Precision microstep actuators drive the platform about the two gimbal axes. Mounted on the platform is a charge coupled device (CCD) optical target tracker. Within the host spacecraft is an inertial reference unit containing gyros to measure spacecraft attitude. For comet mission applications, the spacecraft and science platform are protected behind a dust shield. Figure 1 shows a drawing of a typical spacecraft configuration incorporating these features. As shown in the figure, mirrors are used to view around the shield during approach to a comet. Mirror 1, which extends outboard of the shield, is used for viewing the comet during initial acquisition and while completely protected viewing is impossible. This mirror is jettisoned and mirror 2, mounted inboard of the shield, is latched into position when completely protected viewing is possible.

The major elements of the control system design are shown in Fig. 2. This functional block diagram indicates which elements of the system are located on the spacecraft bus or on the science platform. Redundant elements in the design provide a backup in case of failure detected by onboard or ground monitoring. At any time, though, a single processor performs tracking, pointing, and attitude control computations. In some applications, the target tracker image processing function can be off-loaded to a dedicated processor.

The target tracker used in the design has a 10×10 deg field of view. Only a small fraction of the field of view (1×1 mrad) is accessed and read out for track measurements. This speeds the image acquisition time to allow up to a 10-Hz sampling frequency. Figure 3 shows a block diagram of the target tracker. Reference 2 provides more detail about tracker design and performance.

The precision microstep actuators consist of a harmonic drive to provide a 100:1 reduction through a stiff low-hysteresis coupling, microstep-controlled stepper motor, and associated angle transducers. This actuator provides fine step resolution (5 μrad) and high peak slew rates (>6 deg/s). Reference 3 provides more detail about actuator design and performance.

Trajectory errors determine the need for closed-loop target tracking. After the latest navigation estimates prior to encounter are processed, downtrack trajectory uncertainties far outweigh the crosstrack uncertainty (±700 km vs ±100 km, 1σ). For the purpose of this design study, the combination of a close approach altitude of 1000 km and a flyby relative velocity of 60 km/s will be assumed.

A typical mission would follow the following sequence. Several hours before closest approach the spacecraft is oriented to align the science platform axes so that the axis of major motion is the azimuth axis. This orientation is also

Presented as Paper 82-1617 at the AIAA Guidance and Control Conference, San Diego, Calif., Aug. 9-11, 1982; received Sept. 9, 1982; revision received Sept. 15, 1983.

*Member of Technical Staff, Guidance and Control Section.
†Member of Technical Staff.
‡Member of Technical Staff. Member AIAA.

chosen to place the protective dust shield forward to absorb oncoming dust particles for comet missions. Until the target is initially acquired, the best estimate of the pointing profile based on navigation data is followed. During this time, the whole tracker field of view is searched in a spiral pattern. Once target acquisition has occurred, recursive estimation, explained more fully in the section that follows, is used to improve target trajectory knowledge.

When a large dust particle disturbance causes loss of the target, the last best estimate of target trajectory parameters is used to propagate forward science platform commands until target reacquisition has occurred. If necessary, a spiral search of the whole tracker field of view is performed.

Control System Design

The design of the control system is greatly influenced by the capacity of the onboard processor. To achieve a high pointing accuracy and yet not to exceed the capability of the onboard computer, the control function is divided into base body attitude control and science platform pointing control. The mass properties of the spacecraft and the gimbal axes of the science platform are chosen so that the interaction between the base body control and the platform control is minimized. Furthermore, the orientation of the base body is aligned so that only one of the science platform actuators (azimuth control axis) is required to perform a large-scale articulation during the encounter while the excursion of the other control axis (elevation control axis) is within ±20 deg range. In this way, the science platform pointing control system is "decoupled" into azimuth and elevation controllers.

In the following sections, the required science platform azimuth (AZ) and elevation (EL) angular positions and rates for precise pointing are derived in terms of spacecraft attitude and location in the target coordinate frame. Since the trajectory of the spacecraft, in general, cannot be exactly determined, a trajectory parameter estimator is designed using the measurements obtained by the optical target tracker. The spacecraft attitude is controlled by three decoupled, single-axis, bang-bang control loops using gyros as reference. The attitude control system has two modes of operation: one for small attitude errors (<1 deg), the other for large attitude errors (<20 deg). The former is used for precise science platform pointing while the latter is needed to ensure that precise pointing can be re-established after impact by large dust particles, a possibility near comets. The control design for such missions is usually constrained to an attitude error of less than 20 deg. Otherwise, onboard science instruments will be exposed and damaged by dust particle impact.

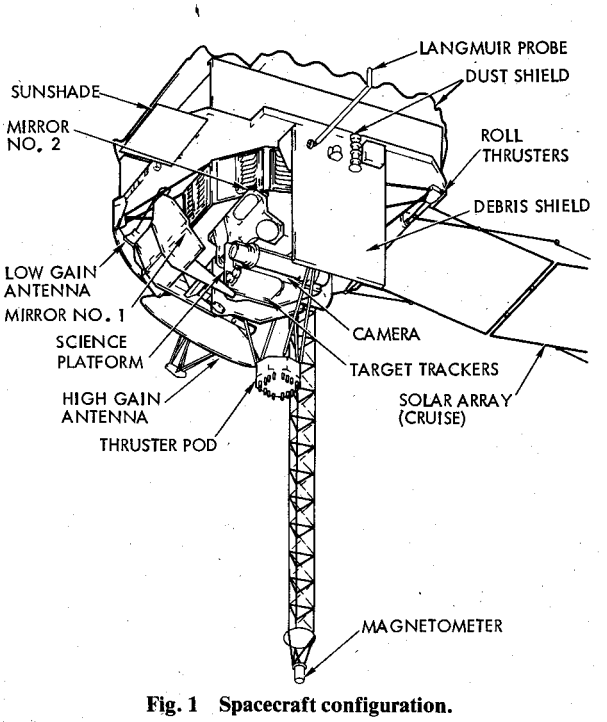

Fig. 1 Spacecraft configuration.

Conditions for Precise Science Platform Pointing

In this section, the required science platform pointing commands in terms of spacecraft trajectory and spacecraft attitude are derived. In order to illustrate the basic approach and yet not to complicate the expressions, the mirrors used in viewing the target for comet encounter applications are omitted in the following derivations. However, equations with mirror configuration will be used in the simulation. The coordinate systems used in the derivation are defined in Fig. 4.

A target coordinate system (x_T, y_T, z_T) is defined so that its origin is coincident with the center of the target, its z_T axis is parallel to the relative velocity vector v of the spacecraft with respect to the target, and its x_T axis is perpendicular to the nominal flyby plane pointing in the direction so that the spacecraft flyby altitude is always in the positive y_T direction. Let $[X_0, Y_0, Z(t)]$ be the location of the spacecraft at time t with respect to the target coordinate frame, and let (x_s, y_s, z_s) be a spacecraft body-fixed coordinate frame which is parallel to the target frame at null attitude error. The target line of sight vector $[\ell_s, m_s, n_s]^T$ can be expressed in spacecraft body-fixed coordinates as

$$\begin{bmatrix} \ell_s \\ m_s \\ n_s \end{bmatrix} \cong \begin{bmatrix} 1 & \theta_z & -\theta_y \\ -\theta_z & 1 & \theta_x \\ \theta_y & -\theta_x & 1 \end{bmatrix} \begin{bmatrix} X_0 \\ Y_0 \\ Z(t) \end{bmatrix} \quad (1)$$

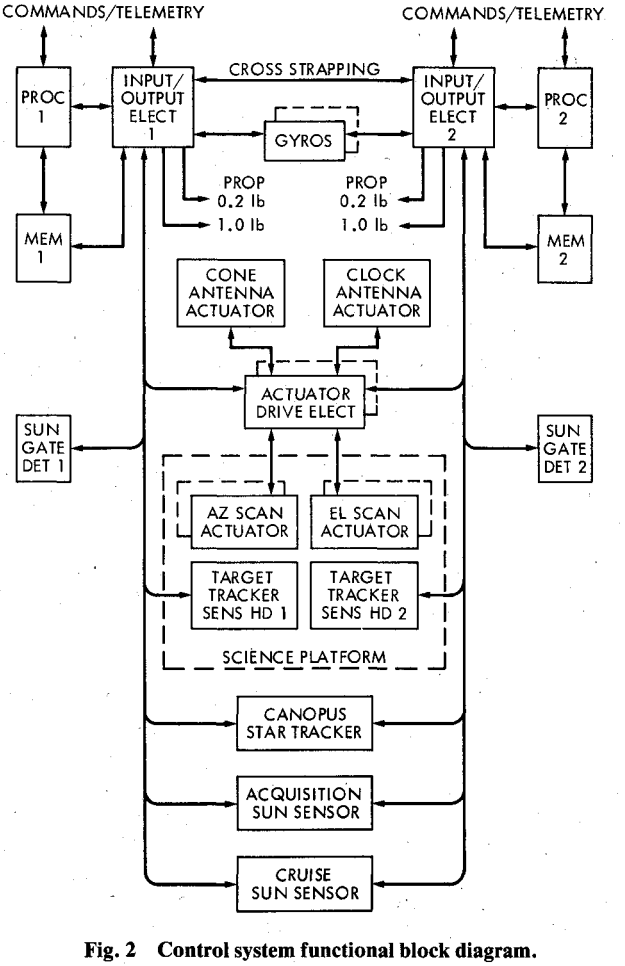

Fig. 2 Control system functional block diagram.

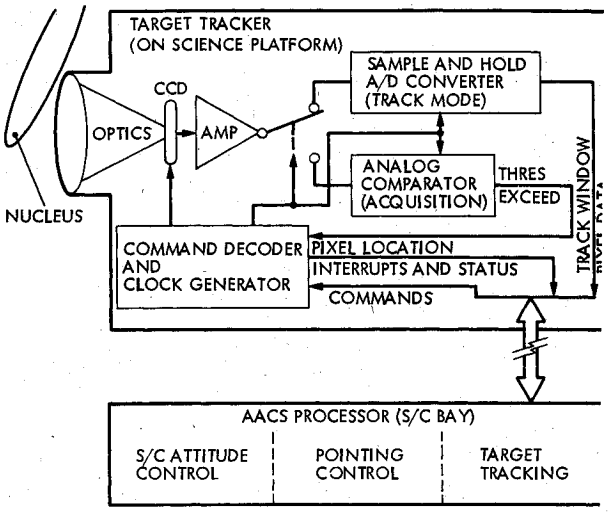

Fig. 3 Target tracker block diagram.

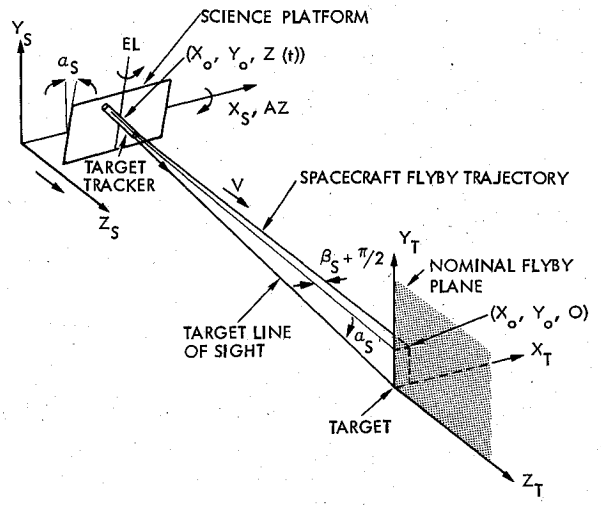

Fig. 4 Coordinate system and flyby geometry.

The angles θ_x, θ_y, and θ_z are the pitch, yaw, and roll attitude errors of the spacecraft, which are assumed to be small. The science platform has two degrees of freedom. It can articulate around the azimuth (AZ) axis, which is parallel to the x_s axis, and it can also articulate around the elevation (EL) axis, which is perpendicular to the AZ axis and is parallel to the y_s axis at zero AZ angle. Let (x_p,y_p,z_p) be the platform body-fixed coordinates which are initially coincident with the spacecraft coordinates (x_s,y_s,z_s). The target line of sight can be expressed in platform coordinates as

$$\begin{bmatrix} \ell_p \\ m_p \\ n_p \end{bmatrix} = \begin{bmatrix} \cos\beta_s & \sin\alpha_s\sin\beta_s & -\cos\alpha_s\sin\beta_s \\ 0 & \cos\alpha_s & \sin\alpha_s \\ \sin\beta_s & -\sin\alpha_s\cos\beta_s & \cos\alpha_s\cos\beta_s \end{bmatrix} \begin{bmatrix} \ell_s \\ m_s \\ n_s \end{bmatrix} \tag{2}$$

where ℓ_p, m_p, and n_p are the components of the target line-of-sight vector in platform coordinates, and α_s and β_s are the gimbal angles of the AZ and EL control axes, respectively. The target tracker is pointed along with the x_p axis. Therefore, for precise pointing, the following conditions must be satisfied:

$$m_p = n_p = 0 \tag{3}$$

or

$$\alpha_s = \tan^{-1}(-m_s/n_s) \tag{4}$$

and

$$\beta_s = -\pi/2 - \tan^{-1}(\ell_s/\sqrt{m_s^2+n_s^2}) \tag{5}$$

Equation (5) was derived using Eqs. (2) and (4). The above relations can also be expressed in terms of spacecraft attitude and trajectory in the target coordinates (x_T,y_T,z_T). Defining the trajectory parameters α and β as

$$\alpha \triangleq \tan^{-1}(-Y_0/Z) \tag{6}$$

and

$$\beta \triangleq -\pi/2 - \tan^{-1}(X_0/\sqrt{Y_0^2+Z^2}) \tag{7}$$

it can be shown that

$$\alpha \cong \alpha_s + \theta_x \tag{8}$$

and

$$\beta \cong \beta_s + [\theta_y\cos\alpha + \theta_z\sin\alpha] \tag{9}$$

The above derivations have used the identity

$$\tan(A-B) = (\tan A - \tan B)/(1+\tan A\tan B) \tag{10}$$

as well as the equalities defined in Eqs. (2), (4), and (5). Furthermore, it is assumed that the flyby altitude Y_0 is much larger than flyby uncertainty X_0 in absolute value. From Eqs. (6-9), the required science platform articulation rate can also be expressed in terms of spacecraft location and attitude:

$$\dot{\alpha}_s = V/Y_0\sin^2\alpha - \omega_x \tag{11}$$

$$\dot{\beta}_s = 0.5(ZV)/(Y_0^2+Z^2)\sin(2\beta) - [\omega_y\cos\alpha + \omega_z\sin\alpha] + \alpha[\theta_y\sin\alpha - \theta_z\cos\alpha] \tag{12}$$

where the relation $\dot{Z} = V(=|v|)$ was used in the above derivation. For the case in which the trajectory of the spacecraft with respect to the target is perfectly known, Eqs. (8), (9), (11), and (12) can be directly applied with the additional information from the attitude control system to point the platform precisely towards the target.

Trajectory Estimation

In most cases, however, the trajectory of the spacecraft relative to the target is not exactly known, and, therefore, must be estimated. This can be done by "measuring" the trajectory parameters α and β which can be obtained by the relations

$$\alpha_m = \alpha_a + \theta_x + \theta_\alpha + \eta_1 \tag{13}$$

and

$$\beta_m = \beta_a + [\theta_y\cos\alpha + \theta_z\sin\alpha] + \theta_\beta + \eta_2 \tag{14}$$

In the above equations, the subscript m is introduced to indicate the "measurement" quantities. The signals θ_α and θ_β are outputs from the target tracker and are generated according to the following relations:

$$\theta_\alpha \triangleq \tan^{-1}(m_p/\ell_p) \tag{15}$$

and

$$\theta_\beta \triangleq \tan^{-1}(-n_p/\ell_p) \tag{16}$$

where ℓ_p, m_p, and n_p are the components of target line of sight defined in Eq. (2). The signals θ_α and θ_β have a maximum value of 1 mrad as limited by the tracker field of view. The terms η_1 and η_2 are introduced to account for approximation error and measurement noise. Notice that in Eq. (13) a factor $\sin\beta_a$ was deliberately omitted from the term θ_α. This is because β_α will vary only slightly from the value of $-\pi/2$ for the particular given flyby geometry and the coordinate systems chosen. The omission of this factor makes the measurement of α mathematically independent of the parameter β. The rates of change of the parameters α and β can be directly derived from Eqs. (6) and (7)

$$\dot{\alpha}=D\sin^2\alpha \tag{17}$$

and

$$\dot{\beta}=0.5(ZV)/(Y_0^2+Z^2)\sin(2\beta) \tag{18}$$

where D is defined as

$$D\triangleq V/Y_0 \tag{19}$$

Equations (13-19) form an estimation problem: based on the measurements, α_m and β_m, and the dynamic equations given in Eqs. (17) and (18), estimate α and β. Because of the fact that the parameter α only involves an additional parameter D in form, α is first estimated. A least-squares criterion approach given in Ref. 4 is used to obtain the result. The estimator is found to have the form

$$\dot{\hat{\alpha}}=D\sin^2\hat{\alpha}+K_1(\alpha_m-\hat{\alpha}) \tag{20}$$

and

$$\dot{\hat{D}}=K_2(\alpha_m-\hat{\alpha}) \tag{21}$$

where the caret represents an estimated value and K_1 and K_2 are the gains of the estimator. The gains are selected primarily on the basis of transient response of the estimator. During the transient, the observation errors η_1 and η_2 given in Eqs. (13) and (14) can be neglected. By defining the estimation errors as

$$\alpha_e=\alpha-\hat{\alpha} \tag{22}$$

and

$$D_e=D-\hat{D} \tag{23}$$

the following equations are obained from Eqs. (17) and (19-21).

$$\dot{\alpha}_e=D\sin^2\alpha-\hat{D}\sin^2\hat{\alpha}-K_1\alpha_e \tag{24}$$

and

$$\dot{D}_e=-K_2\alpha_e \tag{25}$$

Equation (24) can be rewritten as

$$\dot{\alpha}_e=D_e\sin^2\hat{\alpha}+D[\sin^2\alpha-\sin^2\hat{\alpha}]-K_1\alpha_e \tag{26}$$

For the case $\hat{\alpha}\cong\alpha$, the above equation can be further simplified

$$\dot{\alpha}_e=-(K_1-D\sin 2\hat{\alpha})\alpha_e+D_e\sin^2\hat{\alpha} \tag{27}$$

Equations (25) and (27) form a second-order system. The term $D\sin 2\hat{\alpha}$ in Eq. (27) can be omitted for $K_1\gg D$. The term $\sin^2\hat{\alpha}$ varies slowly with time; the maximum percentage of change for this term is calculated to be less than 3%/s. Therefore, $\sin^2\hat{\alpha}$ is considered to be "constant." With these assumptions, the characteristic equation for the seond-order system can be expressed as

$$(\lambda+K_1)\lambda+K_2\sin^2\hat{\alpha}=0 \tag{28}$$

or

$$\lambda=[-K_1\pm\sqrt{K_1^2-4K_2\sin^2\hat{\alpha}}]/2 \tag{29}$$

In the above equations, parameters K_1 and K_2 determine the time constant (or bandwidth and damping factor) of the second-order system. By selecting K_2 according to the relation

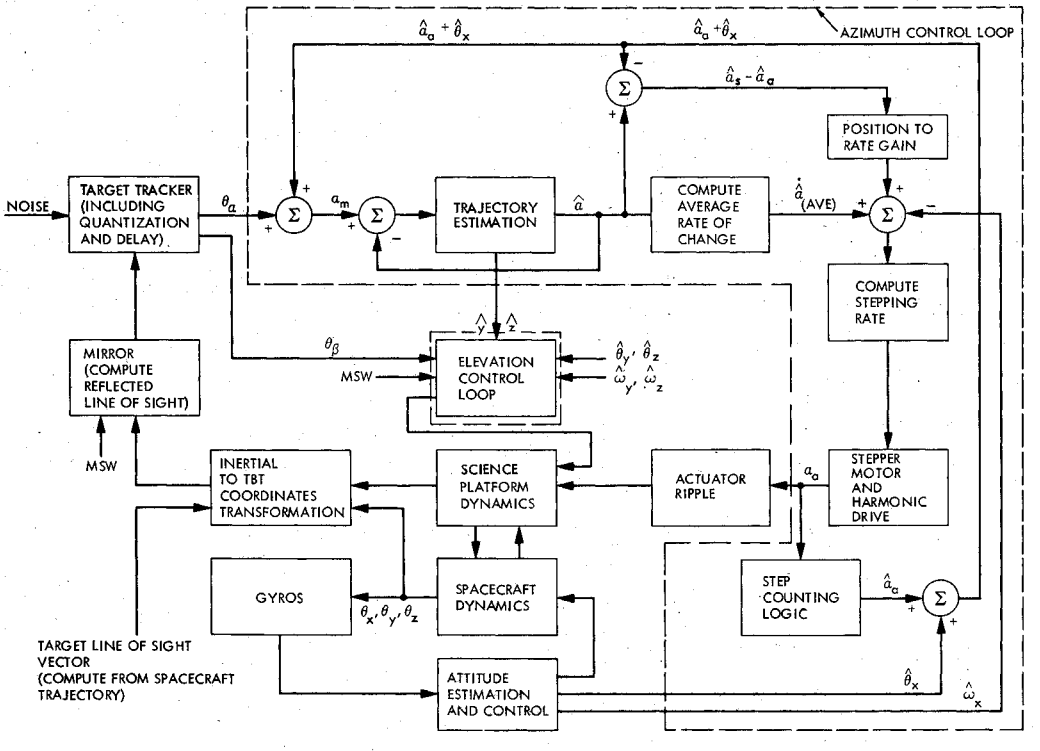

Fig. 5 Control system block diagram.

$$K_2 = 0.5\ K_1^2/\sin^2\hat{\alpha} \tag{30}$$

a damping factor of approximately 0.707 can be obtained. K_2 is further constrained to be less than 50 for small values of $\hat{\alpha}$. The parameter K_1 is determined to be in the range of 0.2 to 1.0 based on the simulation studies. The parameter β is estimated from the following equation.

$$\dot{\hat{\beta}} = 0.5\ \hat{Z}V/(\hat{Z}^2 + \hat{Y}_0^2)\sin(2\hat{\beta}) + K_3(\beta_m - \hat{\beta}) \tag{31}$$

where $\hat{\beta}$ is the estimated value of β

$$\hat{Y}_0 = V/\dot{D} \tag{32}$$

and

$$\hat{Z} = \hat{Y}_0/(\tan\hat{\alpha}) \tag{33}$$

The gain K_3 is set to be 0.2, again based on simulation studies.

Science Platform Pointing Control

Using the estimated spacecraft trajectory parameters, α, β, X_0, Y_0, and $Z(t)$, the desirable science platform AZ and EL angular positions (α_s and β_s) and rates ($\dot{\alpha}_s$ and $\dot{\beta}_s$) for precise pointing can be computed from Eqs. (8), (9), (11), and (12). These desirable positions and rates can be achieved if the commanded science platform AZ and EL slew rates $\dot{\alpha}_a$ and $\dot{\beta}_a$ are set according to the following expressions:

$$\dot{\alpha}_a = \dot{\alpha}_s + G_1(\alpha_s - \alpha_a) \tag{34}$$

and

$$\dot{\beta}_a = \dot{\beta}_s + G_2(\beta_s - \beta_a) \tag{35}$$

where α_a and β_a are the actual science platform AZ and EL positions based on the information of AZ and EL actuator step counts. The commanded rates $\dot{\alpha}_a$ and $\dot{\beta}_a$ are slightly deviated from the computed $\dot{\alpha}_s$ and $\dot{\beta}_s$ in order to correct the position offsets from the desired positions α_s and β_s. The selection of the gains G_1 and G_2 depends on the required convergence rate of the pointing control system, the actual rate command resolution, and the sampling rate. The procedure for generating the onboard actuator rate command for the AZ axis is the following:

1) Estimate $\hat{\alpha}(n+1)$, based on target tracker output, θ_α, and the current estimate of the parameter $\hat{\alpha}(n)$, where n is the current sampling time.

2) Compute the AZ pointing error based on the estimated spacecraft attitude error at time n, $\hat{\theta}_x(n)$, the actual scan platform AZ position measured by step counting logic, $\hat{\alpha}_a(n)$, and the estimated $\alpha(n)$.

3) Compute the desired average AZ actuator slew rate during the period $(n,n+1)$ based on $\hat{\alpha}(n)$ and $\hat{\alpha}(n+1)$.

4) Generate the required slew rate by taking into consideration the estimated spacecraft limit cycle rate ω_x and the AZ pointing error.

5) Compute $\hat{Y}_0(n)$ and $\hat{Z}(n)$ for the β estimator.

The procedure for generating the rate command for the EL control axis is similar to the above except that the spacecraft limit cycle compensation is slightly more involved. A detailed control system block diagram is shown in Fig. 5. All symbols shown in the block diagram have been defined earlier, except the symbol MSW, which is needed to accommodate mirror switching and is incorporated in the simulation section. In computing the desired science platform positions and rates, the base body attitude information was assumed [see Eqs. (8), (9), (11), and (12)]. It was also assumed that throughout the science platform pointing mode, the attitude errors of the base body are small. For large errors, the science platform control is temporarily disabled until the base body attitude error can be recovered, as discussed in the following.

Spacecraft Attitude Control Design

A dual-mode attitude control scheme is designed for the spacecraft base body. This control scheme involves using a specified parabolic switching curve during high rates, and returning to a straight switching line whenever the estimated attitude error falls within a selected controller deadband. The parabolic switching line is chosen such that the transient response time resulting from dust impacts can be minimized. This minimal-time control scheme is implemented primarily for comet encounters during which collisions with large dust particles are quite probable, and rapid spacecraft attitude recovery is crucial.

Base Body Attitude Control

A three-axis stabilized controller is designed for the base body. The switching line for controlling each axis is defined by

$$\theta = K\omega \pm \mathrm{DB} \tag{36}$$

where θ and ω are the position and rate errors, K is the rate-to-position gain, and DB is the control deadband size. The position error θ, is obtained from the gyro output measurements. The rate for each axis ω is computed by the estimator

$$\omega(t) = G_3\omega(t_0) + G_4(\theta(t) - \theta(t_0))/\Delta t, \qquad t = t_0 + \Delta t \tag{37}$$

where G_3 and G_4 are the estimator gains and Δt is the gyro sampling period. The control error, ϵ, for each axis is computed from Eq. (36).

$$\epsilon = \theta - K\omega \tag{38}$$

The control law is a bang-bang type, defined as follows:

If

$$\epsilon \begin{cases} > \mathrm{DB} \\ < \mathrm{DB} \\ \text{otherwise} \end{cases} \quad \text{then, torque polarity:} \quad \begin{cases} - \\ + \\ \text{thrusters not enabled} \end{cases}$$

The above control law is normally active when the base body is limit-cycling at low rates.

However, in the event that the spacecraft is impacted by large dust particles, the instantaneous rate is high while the position error is still small. The resulting trajectory as seen on the phase plane AB in Fig. 6 is a function of the moment of inertia and the thruster torque about that axis. At B, the thrusters are turned off as soon as the error falls within the deadband ($\pm$DB). However, since the rate is negative at B, the spacecraft will move in the direction of reducing the position error, exit the deadband, cause thruster firings, re-enter the deadband, and so forth. This process of repeatedly crossing in and out of the lower deadband edge, and hence, a sequence of repeated thruster firings, results in slow attitude recovery and long transient response time.

Minimal-Time Control Law

The idea of minimal-time control is to command the thrusters to be fired continuously by bringing the errors to the origin without interruption by repeated crossings of the deadband edge. In essence, it is desirable to have a control law which commands the thrusters to reverse polarity at an optimal time in order to achieve the above purpose.

Given a constant control torque, the rate-position trajectory of the spacecraft response is parabolic on the phase plane. The parabola is derived as follows: Let θ_0 be the initial position error, γ the acceleration, and t the time variable, then

for each axis,

$$\omega = \gamma t$$

and

$$\theta = \tfrac{1}{2}\gamma t^2 + \theta_0 \tag{39}$$

The initial rate error is usually quite small, and is assumed negligible here. From Eq. (39), we obtain

$$\theta = \omega^2/2\gamma + \theta_0 \tag{40}$$

which defines the parabola for the control switching line for some value θ_0.

A minimal-time control law is designed based on the above parabolic switching line. The curvature of the switching line should follow that of the rate-position trajectory, as shown by line C-0 in Fig. 6, such that when the thrust polarity is reversed, the rate-position error will be brought to the origin without deadband crossings. From Eq. (40), the control switching line for each axis is as follows:

$$\theta = G\omega^2 \operatorname{sgn}(\omega) \pm \mathrm{DB} \tag{41}$$

where

$$\operatorname{sgn}(\omega) = \begin{cases} 1, & \omega > 0 \\ -1, & \omega < 0 \end{cases}$$

and $G = -I/2T$, where I and T are the moment of inertia and thruster torque about one axis, respectively. The $\operatorname{sgn}(\omega)$ function is to ensure that the switching line is lying in the proper quadrant on the phase plane. The minimal-time control law computes the error ϵ by

$$\epsilon = \theta - G\omega^2 \operatorname{sgn}(\omega) \tag{42}$$

To measure the large attitude errors during attitude recovery, a quaternion or Euler parameter integrator algorithm is implemented. This quaternion technique is preferred over the direction cosine method for two basic reasons. First, the quaternions have no inherent geometrical singularity (undefined values) which can occur for the direction cosine representation. Second, the quaternion representation has only four parameters, in contrast to Euler's nine, and, hence, does not require as much processing time or storage for attitude computation.

The quaternion $q = [q_1, q_2, q_3, q_4]^T$ represents a rotation from the spacecraft coordinates $[x_s(t), y_s(t), z_s(t)]$ to the target coordinates. It is defined by

$$q = q_1 i + q_2 j + q_3 k + q_4$$

where i, j, k are unit vectors, and q has the property $q_1^2 + q_2^2 + q_3^2 + q_4^2 = 1$. The quaternion integrator used for propagating q over time is derived by directly using the incremental position vector $p(t)$ measured by the gyros. The quaternion integrator as a function of a rate quaternion $\Omega(t) = [w(t), 0]$, where $w(t)$ is the spacecraft rate, is a solution of the differential equation

$$\dot{q}(t) = \tfrac{1}{2}\Omega(t) q(t) \tag{43}$$

The quaternion multiplication in Eq. (43) is defined by the following operation:

$$\Omega q = \begin{bmatrix} \Omega_4 & \Omega_3 & -\Omega_2 & \Omega_1 \\ -\Omega_3 & \Omega_4 & \Omega_1 & \Omega_2 \\ \Omega_2 & -\Omega_1 & \Omega_4 & \Omega_3 \\ -\Omega_1 & -\Omega_2 & -\Omega_3 & \Omega_4 \end{bmatrix} \begin{bmatrix} q_1 \\ q_2 \\ q_3 \\ q_4 \end{bmatrix} \tag{44}$$

for $\Omega = (\Omega_1, \Omega_2, \Omega_3, \Omega_4)^T$. The solution expressed as a difference equation in terms of $\Omega_0 \triangleq \Omega(t_0)$ is

$$q(t) = [[0\ 0\ 0\ 1]^T + \tfrac{1}{2}\Omega_0 \Delta t + (\tfrac{1}{2}\dot{\Omega}_0 + \tfrac{1}{4}\Omega_0^2)\Delta t^2/2 + (\tfrac{1}{2}\ddot{\Omega}_0 + \tfrac{1}{4}\dot{\Omega}_0\Omega_0 + \tfrac{1}{2}\Omega_0\dot{\Omega}_0 + \tfrac{1}{8}\Omega_0^3)\Delta t^3/6 + \ldots] q(t_0) \tag{45}$$

for $t > t_0$, where $\Delta t = t - t_0$ is the gyro sampling period. Defining the gyro output quaternion to be $p(t) = [p(t), 0]$, for the time interval $[t_0, t_0 + \Delta t]$, $p(t)$ can be expressed as:

$$p(t) = \int_0^{\Delta t} \Omega(t)\,dt = \Omega_0 \Delta t + \dot{\Omega}_0 \Delta t^2/2 + \ddot{\Omega}_0 \Delta t^3/6 + \ldots \tag{46}$$

The above integration is over the Taylor series expansion of $\Omega(t)$ about Ω_0. Similarly, the previous gyro output $p(t_0)$ over the interval $[t_0 - \Delta t, t_0]$ is

$$p(t_0) = \Omega_0 \Delta t - \dot{\Omega}_0 \Delta t^2/2 + \ddot{\Omega}_0 \Delta t^3/6 + \ldots \tag{47}$$

From Eqs. (46) and (47), Ω_0, $\dot{\Omega}_0 \ldots$ can be solved in terms of $p(t)$, $p(t_0)$, etc. Assuming the terms containing (Δt^3) are negligible, the following relations are obtained:

$$\Omega_0 = (p(t) + p(t_0))/2\Delta t$$

$$\dot{\Omega}_0 = (p(t) - p(t_0))/(\Delta t)^2 \tag{48}$$

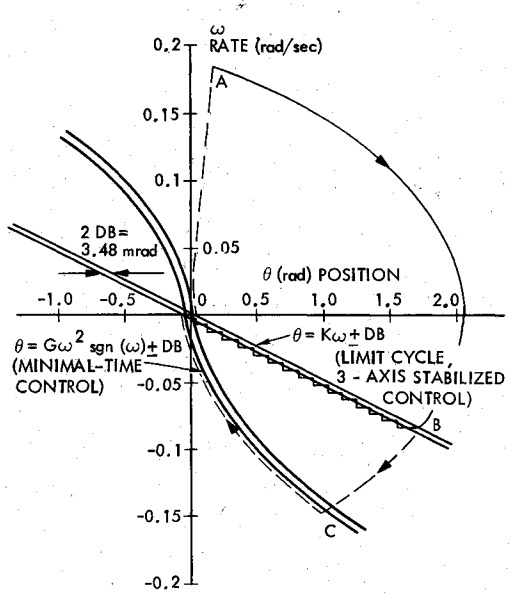

Fig. 6 Base body control law.

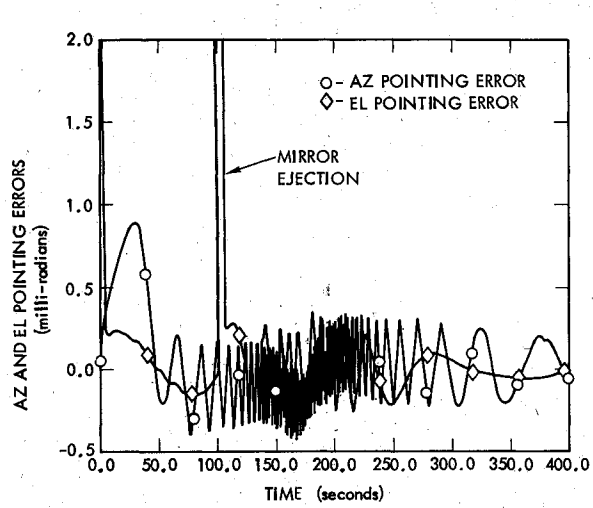

Fig. 7 Trajectory parameter α and science platform AZ angle α_a.

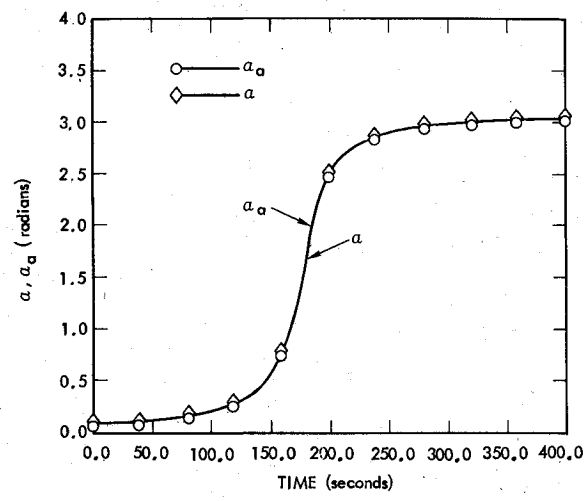

Fig. 8 Trajectory parameter β and science platform EL angle β_a.

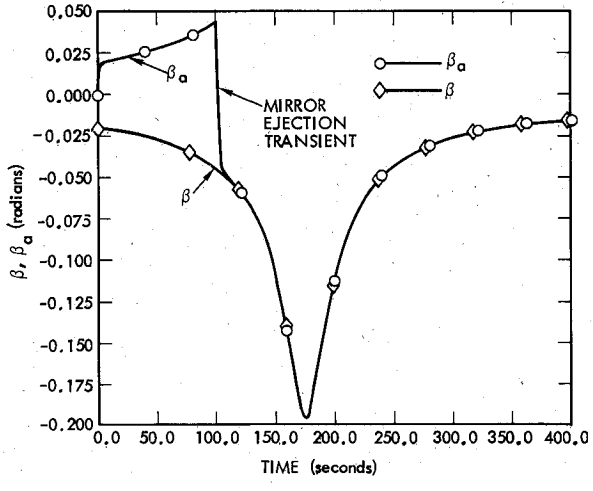

Fig. 9 Science platform pointing error.

From Eq. (45), the quaternion equation used for propagating the spacecraft attitude is obtained.

$$q(t) = [[0001]^T + p(t)/2 + (p(t) + p(t_0))^2/32]q(t_0) \quad (49)$$

The direction cosines of the spacecraft coordinate axes with respect to the target coordinates is a direct function of the quaternion $q(t)$ (Ref. 5). The attitude errors can be expressed in terms of the normalized quaternions as follows:

$$\theta_x = \sin^{-1}[2\,|q_1q_2 - q_3q_4, q_1q_3 + q_2q_4|]$$

$$\theta_y = \sin^{-1}[2\,|q_1q_2 + q_3q_4, q_2q_3 - q_1q_4|]$$

$$\theta_z = \sin^{-1}[2\,|q_1q_2 - q_2q_4, q_2q_3 + q_1q_4|] \quad (50)$$

where $|a,b| \triangleq \sqrt{(a^2+b^2)}$

Dual-Mode Attitude Control

The minimal-time control law is to be activated only when the spacecraft induced rate is high; otherwise, unstable limit cycling would result. This is because the parabolic switching line cannot be employed when rate-position error is near the origin where the curves are tangential to the ω axis. For this reason, a dual-mode control scheme for each axis is proposed as follows:

Minimal-time mode: $|\omega| \geq \omega_T$ or $|\theta| \geq \theta_T$

$$\epsilon = \theta - G\omega^2 \mathrm{sgn}(\omega)$$

Other modes: $\epsilon = \theta - K\omega \quad (51)$

where ω_T and θ_T are specified rate and position thresholds.

Simulation and Performance Assessment

To evaluate the pointing performance of the control system, the scheme presented in the previous sections was simulated on the computer using a six-body spacecraft model (main body, science platform azimuth, science platform elevation, solar array, high-gain antenna, and magnetometer boom.) As a preliminary study, the magnetometer boom is modeled by a hinge-connected rigid body having the characteristics of the fundamental mode frequency (2.4 Hz) and low (0.5%) damping. Also included in the simulation program are the two mirrors previously described. Mirror 2 will be deployed for comet viewing at approximately 100 s before closest approach. The equations pertaining to the EL control axis (parameter β) derived earlier were modified to accommodate the change. Equations related to mirrors 1 and 2 are combined using a logical variable MSW which is set to "zero" for mirror 1 and "one" for mirror 2. The modified equations in the simulation were executed at 125 ms intervals. It was found that for sampling time intervals of 125 ms or less, the differential equations used for the control scheme can be approximated by first-order difference equations (not shown), with no appreciable error.

The simulation results of the science platform pointing performance are summarized in Figs. 7-9. Figure 7 shows the values of estimated α (which is also the desired science platform angle at null base body attitude error) and the actual science platform AZ actuator position α_a during the flyby. These two curves match perfectly to the level of plotter resolution. Both α and α_a angles vary 180 deg during the flyby. The value of estimated β is shown in Fig. 8. This parameter deviates slightly from $-\pi/2$ rad due to out-of-plane error. (In the figure, the value of only β is shifted up by $\pi/2$ rad.) The angle β reaches a peak at the closest approach time (at $t = 175$ s). The corresponding platform EL position β_a is shown in the same figure. The angle of β_a differs from the angle β by approximately $-\pi/2$ rad due to the effect of the mirrors. The EL actuator position is flipped over at $t = 100$ s because of mirror jettison. During the transient of mirror jettison (for a few seconds), while the target was out of the tracking field of view, the error signals from the target tracker were temporarily inhibited and the desired science scan platform positions and rates were computed in open-loop fashion. The target tracker error signals were used again when the target was reacquired. The AZ and EL pointing errors of the platform are shown in Fig. 9. Except during pointing initialization and mirror switchover, the pointing error was generally within 0.5 mrad. The major contributor to the pointing error was due to the actuator ripple which has an amplitude of ± 0.24 mrad (included in the model). The "steady-state" rate error was shown to be on the order of 2 mrad/s. The spacecraft attitude error during the flyby is limit-cycling within a ± 1.74 mrad deadband, and it has been shown that the attitude error has no significant effect on the pointing accuracy. Therefore, the overall performance is considered to be satisfactory.

The effect of a large dust particle impact has also been investigated. The spacecraft initial conditions are set such that the base body is in a quiescent state. Then a large particle traveling at a relative velocity of 60 km/s impacts at the dust shield transferring all of its momentum to the spacecraft

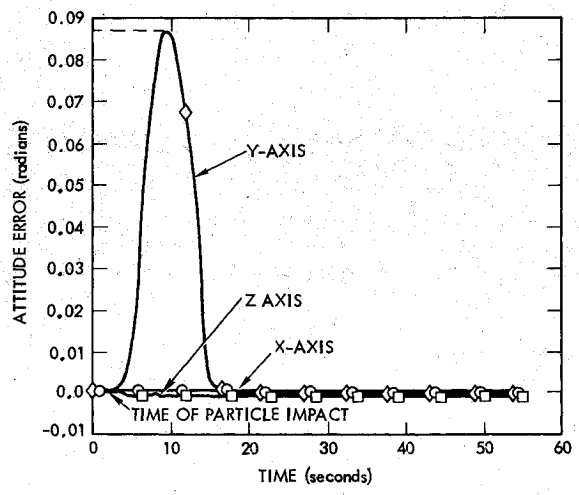

Fig. 10a Base body attitude error from particle impact.

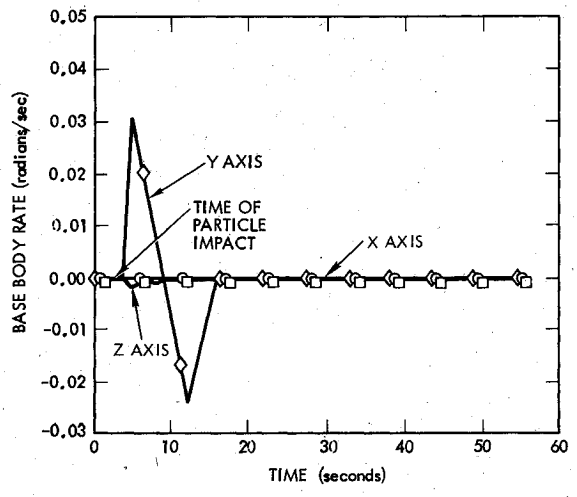

Fig. 10b Base body rate response from particle impact.

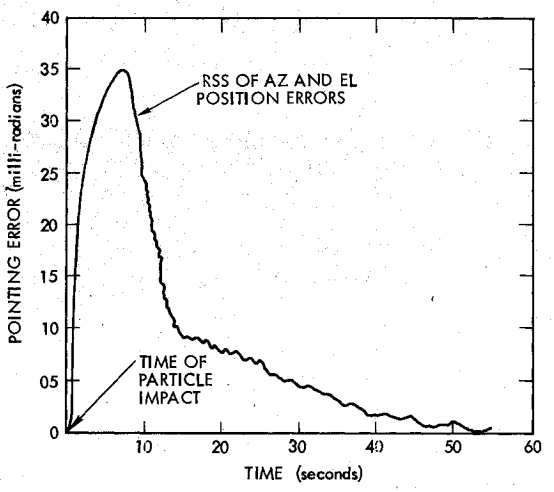

Fig. 11a Science platform position error from particle impact.

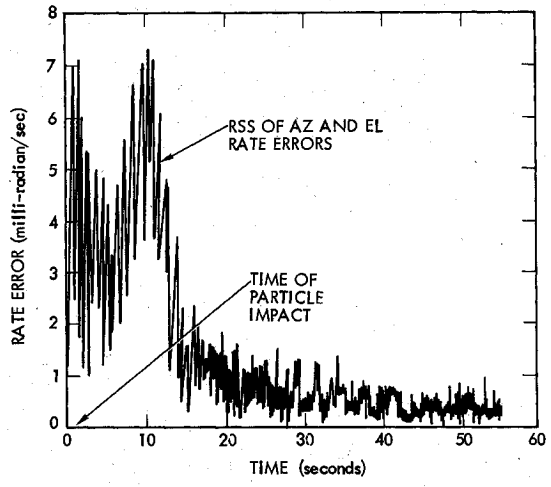

Fig. 11b Science platform rate error from particle impact.

about the *Y* axis, causing a maximum angular error of 5 deg and a rate error of 1.8 deg/s about that axis (Figs. 10a and 10b). Meanwhile, with the minimal-time control enabled, the control thrusters are pulsing at 20-ms intervals to reduce the attitude error within the deadband (DB), all occurring within a period of 15 s. The science platform position and rate errors during and after particle impact are shown in Figs. 11a and 11b. After recovery to the original attitude, and return of the spacecraft to steady state, the pointing stability has been shown to achieve a 10-μrad bounded error within any 1-s interval. Furthermore, after the celestial target has been reacquired, the residual science platform pointing error shows no sign of sustained oscillations.

Conclusion

The tracking and pointing system described in this paper is shown to meet the need of a wide range of high-velocity comet, asteroid, and small planetary moon flyby encounter missions planned in the next decade. This is supported by dynamic simulations with realistic component models. For comet missions, where dust particle impact disturbances are involved, special control measures are required.

Acknowledgments

This paper represents the results of one phase of research carried out at the Jet Propulsion Laboratory, California Institute of Technology, under contract with the National Aeronautics and Space Administration.

References

[1]Key, R.W., "A Spacecraft Attitude and Articulation Control System Design for the Comet Halley Intercept Mission," AIAA Paper 81-0193, Aug. 1981.

[2]Armstrong, R.W. and Shalom, E., "Experimental Verification of CCD-Based Optical Target Tracking Performance," AIAA Paper 82-1619, Aug. 1982.

[3]Marchetto, C.A., "Precision μ-Stepping Actuator," *Eleventh Annual Symposium on Incremental Motion Control Systems and Devices,* Chicago, Ill., May 1982.

[4]Detchmendy, D.M. and Sridhar, R., "Sequential Estimation of States and Parameters in Noisy Nonlinear Dynamical Systems," *Journal of Basic Engineering,* Vol. 88, June 1966, pp. 362-368.

[5]Grubin, C., "Derivation of the Quaternion Scheme via the Euler Axis and Angle," *Journal of Spacecraft and Rockets,* Vol. 7, Oct. 1970, p. 1261.